Journal of Hazardous Materials 193 (2011) 194–199

Contents lists available at ScienceDirect

Journal of Hazardous Materials

journal homepage: www.elsevier.com/locate/jhazmat

# Solid state synthesis of tin-doped ZnO at room temperature: Characterization and its enhanced gas sensing and photocatalytic properties

Xiaohua Jia[a,b], Huiqing Fan[a,*], Mohammad Afzaal[b,d], Xiangyang Wu[c], Paul O'Brien[b,*]

[a] State Key Laboratory of Solidification Processing, School of Materials Science and Engineering, Northwestern Polytechnical University, Xi'an 710072, China
[b] School of Chemistry and School of Materials, University of Manchester, Oxford Road, Manchester M13 9PL, UK
[c] School of the Environment, Jiangsu University, Xuefu Rd. 301, Zhenjiang 212013, Jiangsu, China
[d] Institute of Research Excellence in Renewable energy, King Fahd University of petroleum and Mineral, PO Box 1292, Dhahran 31261, Saudi Arabia

ARTICLE INFO

*Article history:*
Received 18 February 2011
Received in revised form 12 July 2011
Accepted 12 July 2011
Available online 20 July 2011

*Keywords:*
Low temperature solid state reaction
Tin-doped ZnO
Gas response
Photocatalysis

ABSTRACT

A room temperature solid-state reaction has been used to prepare crystalline tin-doped ZnO. Zinc nitrate hexahydrate, cetyltrimethyl ammonium bromide, stannic chloride pentahydrate and sodium hydroxide with proper ratios were ground together. As-synthesized samples were characterized by inductively coupled plasma analysis (ICP), scanning electron microscopy (SEM) and X-ray powder diffraction (XRD); The products were of different morphologies, well dispersed and exhibited good crystallinity, it is also found that the growth direction and morphology of ZnO depend on the amount of Sn doped, which is mainly caused by the difference in sizes between Zn and Sn atoms as well as the change of pH value. Moreover, gas sensing and photocatalytic properties of the obtained products were studied. The materials showed a high gas response to ethanol vapor, and the gas response can reach a maximum of $R_a/R_g = 124$. In addition, tin-doped ZnO materials exhibited improved photocatalytic performance toward methyl orange (MO) solution under a current density of 0.03 mg $L^{-1}$ comparison with undoped ZnO.

© 2011 Elsevier B.V. All rights reserved.

## 1. Introduction

Zinc oxide (ZnO) is a well-known, wide bandgap semiconductor (*Eg* = 3.37 eV at 300 K) and with a large exciton binding energy (60 meV) and has found applications in many devices including: ultrasonic transducers, piezoelectric transducers, varistors, phosphors, catalysts, pigments, photoelectric and UV-absorbers [1–7]. The properties of ZnO can be significantly enhanced by the addition of metal ions as dopants. ZnO can accommodate several types of defects and behave as *n*-type semiconductor due to: oxygen vacancies [8], zinc vacancies [9], O interstitials [10], zinc interstitials [11], and more complex defects [12]. In order to minimize defects, group III, IV and V ions can be doped into ZnO matrix e.g. the substitution of zinc with magnesium results in an increase in the bandgap closer to 4.0 eV, whilst still maintaining the wurtzite structure. A number of studies have appeared which are mainly focused on the doping of ZnO with metal ions including: Fe [13], Ni [14], and Mn [15]. Much of the above work has been devoted to understanding the origin of room temperature ferromagnetism in such systems. Relatively little work exists on Cu, Al, or Cd doped ZnO materials and their resulting optical or electrical properties [5,16,17].

Many synthetic techniques have been employed for the preparation of doped ZnO nanocrystals including: sol–gel processes [18], co-precipitation [19], aqueous solution deposition [20] and mechanochemical processing [21]. However, most of these techniques result in either binary products or products contaminated with the doped metal ion. Several research groups have reported the growth of $SnO_2$–ZnO composites but reports of doping of ZnO with tin are rare. Peiteado et al. [22] have attempted to use a co-precipitation route to obtain tin-doped ZnO materials; however, the resulting material was contaminated with the $Zn_2SnO_4$ spinel phase. Luminescent tin-doped ZnO was prepared by ball milling followed by calcination at a high temperature (1280 °C). Again, XRD results showed the formation of the ternary spinal phase [23]. Fang et al. have reported the successful growth of tin doped ZnO nanobelts at 700 °C in an argon/oxygen atmosphere mixture [24]. There is hence a need for an economical and facile route for the preparation of tin-doped ZnO nanocrystals. Herein, we report a room temperature, solid-state reaction that produces tin-doped ZnO nanocrystals. The reaction is fast and can be initiated by grinding the reactants at or near room temperature and does not require calcination at high temperatures [25]. The gas sensing and photocatalytic properties of the resulting materials have also been investigated.

* Corresponding authors.
*E-mail addresses:* hqfan3@163.com (H. Fan), paul.obrien@manchester.ac.uk (P. O'Brien).

0304-3894/$ – see front matter © 2011 Elsevier B.V. All rights reserved.
doi:10.1016/j.jhazmat.2011.07.049

## 2. Experimental details

### 2.1. Preparation of tin-doped ZnO

Zinc nitrate hexahydrate ($Zn(NO_3)_2{\cdot}6H_2O$), cetyltrimethyl ammonium bromide (CTAB), stannic chloride pentahydrate ($SnCl_4{\cdot}5H_2O$) and sodium hydroxide (NaOH) were of analytical grade and were used as received. All the chemical reagents were purchased from Shanghai Chemical Co. In a typical experiment, $Zn(NO_3)_2{\cdot}6H_2O$ (4.46 g, 1.50 mmol), $SnCl_4{\cdot}5H_2O$ (0.053–1.052 g, 0.015–0.3 mmol) and NaOH (4.0 g, 10 mmol) were blended together in an agate mortar and ground for 10 min at room temperature. Then, CTAB (1.536 g, 0.42 mmol) was added to the mixture and ground for further 50 min. To remove unreacted reactants and by-products, the white mixture was washed several times in turn with distilled water and absolute ethanol. The white products were collected by centrifugation and dried at 60 °C for 10 h. The details of the samples are summarized in Table 1.

### 2.2. Characterization

The phase structure and purity of the as synthesized nanocrystals were examined by X-ray diffraction (XRD, Holland Philips X'pert X-ray diffractometer with Cu-K$\alpha$ radiation, $\lambda = 1.5406$ Å) at 40 kV, 30 mA over the $2\theta$ range 20–80°. Lattice parameters of nanocrystals were calculated according to the formula:

$$\sin^2\theta = \frac{4\lambda^2}{3a^2}\left[h^2 + hk + k^2 + \frac{l^2}{(4c/3a)^2}\right] \quad (1)$$

The surface morphology and size of the different amount of tin-doped ZnO nanocrystals were studied by field-emission scanning electron microscopy (FE-SEM, Zeiss, Germany, supra 55 microscope with an accelerating voltage of 20 kV). Inductively coupled plasma analysis was performed on an inductively coupled plasma atomic emission spectroscopy (ICP-AES, Fisons Horizon, Perkin-Elmer Optima 5300 dual). The specific surface area of all the samples was determined using nitrogen adsorption apparatus (Beckman Coulter SA 3100, BET method).

### 2.3. Gas sensing property measurements

Gas sensor preparation and measurements were carried out by the previously reported method [26]. Measurements on gas response were performed with a static state test system (WS-30A, Winsen Electronics Co. Ltd., Zhengzhou, China).

### 2.4. Photocatalytic measurements

The experiment was carried out with 150 mL Pyrex glass reservoir. The structure of photoreactor used is similar to that in previous report [27]. Methyl orange (MO) in aqueous solution was used as a model contamination to characterize photocatalytic activity at room temperature. Various amounts of the tin-doped ZnO catalyst were placed in a 150 mL MO ($2.0 \times 10^{-5}$ mol $L^{-1}$) solution. The suspension was continuously stirred for 30 min in the dark before irradiation was commenced to allow equilibration at tin-doped ZnO surface. During the irradiation the photoreactor was stirred to maintain a homogeneous suspension. The decolorized solution was subjected to spectra measurement for various times intervals after centrifugation. A blank experiment was performed taking MO solution without photocatalyst to know the extent of decolorization of MO due to 125-W high-pressure mercury lamp (photochemical reactors LTD., Model NO. 3110) alone. This lamp can give maximum wavelength of UVB is $\lambda \geq 315$ nm.

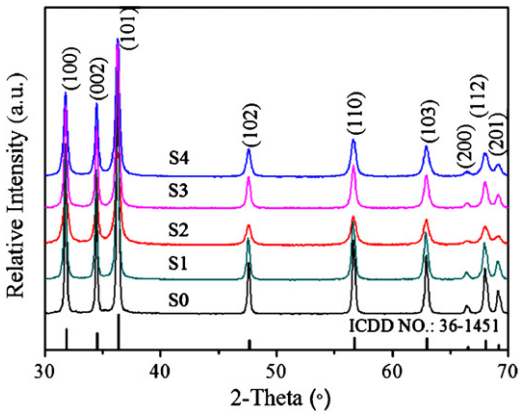


**Fig. 1.** XRD patterns of undoped and with different amount of tin-doped ZnO obtained from room temperature. Standard ZnO pattern (ICCD NO. 36-1451) is given for comparison.

### 2.5. Absorbance measurements

The absorbance of dye solution before and after irradiation was measured at different times. Measurements were carried out using Thermo Spectronic Helios UVB v4.55 spectrophotometer in the photon energy range of wavelength from 350 to 600 nm and with aid of quartz curvettes (Helma) with path length of 1 cm. The percentage of decolorization was calculated from the following formula:

$$D_e\% = \left[1 - \frac{A_t}{A_0}\right] \times 100 \quad (2)$$

where $A_t$ is the absorbance after time $t$ and $A_0$ is the dye initial concentration before decolorization.

## 3. Results and discussion

### 3.1. Microstructure and morphology observations

A low temperature solid state reaction has been carried out for the preparation of tin-doped ZnO crystals. X-ray powder diffraction (XRD) patterns of undoped and tin-doped ZnO crystals revealed the presence of only wurtzitic material (ICDD NO. 36-1451) (see Fig. 1). No other phases such as the often seen $Zn(OH)_2$, $SnO_2$ or $Zn_2SnO_4$ were detected. The diffraction peaks of tin doped ZnO shifted to lower angles, suggesting that the unit cell expands to accommodate

**Table 1**
Calculated lattice parameters ($a$) and ($c$) of undoped and tin-doped ZnO obtained from room temperature.

| Sample no. | Tin added (wt%) | ICP results (wt%) | Lattice parameter ($a$) (Å) | Lattice parameter ($c$) (Å) |
|---|---|---|---|---|
| S0 | 0 | 0 | 3.2452 | 5.1991 |
| S1 | 1% | <0.3% | 3.2524 | 5.2087 |
| S2 | 3% | <0.3% | 3.2561 | 5.2135 |
| S3 | 5% | 0.83% | 3.2596 | 5.2183 |
| S4 | 20% | 1.02% | 3.2618 | 5.2194 |

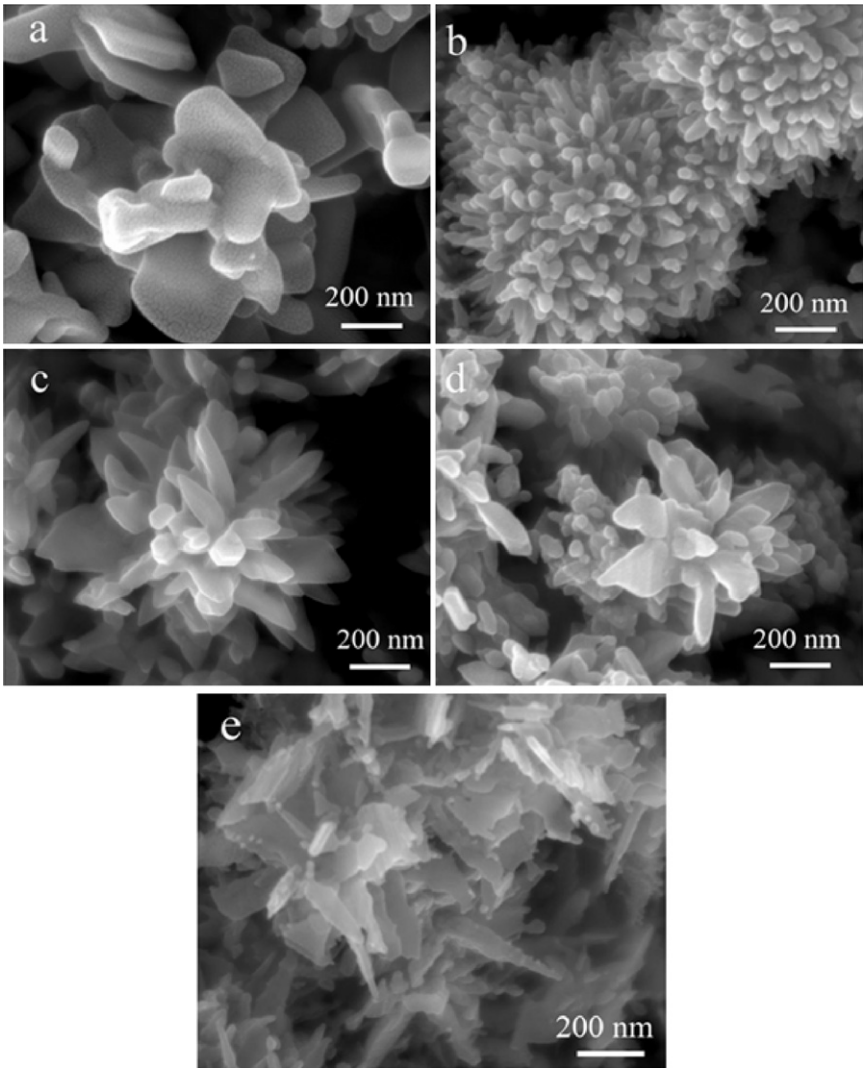


**Fig. 2.** SEM images of (a) undoped ZnO and tin-doped ZnO (b) sample S1, (c) sample S2, (d) sample S3 and (e) sample S4 obtained from room temperature.

the tin. This change is expected on tin replacing zinc ions in the lattice, as the ionic radii are 0.69 Å ($Sn^{4+}$) and 0.60 Å ($Zn^{2+}$). The lattice parameter changes in samples determined from the XRD data and were calculated according to formula (Eq. (1)) and are given in Table 1.

The effect of composition on the microstructure and morphology are shown in Fig. 2. Pure ZnO consisted of large irregular aggregates of sheets as depicted in Fig. 2a. Upon introduction of tin ions into the ZnO matrix, its morphology became more regular and the morphology changed from sheets to clusters of rods (Fig. 2b–d). In sample S4, a flake-like morphology was evident. In another words, the addition of tin elements to ZnO reduces the grain size of ZnO obviously. The resulting morphologies as a function of different Sn concentrations may be attributed to compressive stresses arising from the difference in the sizes of the $Zn^{2+}$ and $Sn^{4+}$ ions [28]. Another reason is that different pH values have an important influence on the morphology of the nanocrystals [29], the pH value changing with the amount of $SnCl_4{\cdot}5H_2O$ added in the experiment, which have a big influence on the morphology of ZnO.

ICP analysis showed that the tin concentration in sample S3 was 0.83 wt% and 1.02 wt% in sample S4 with respect to the amount of $Zn^{2+}$ (see Table 1). Therefore a large fraction of tin was not incorporated into the particles. In order to further understand the above results, another chemical reaction between $SnCl_4{\cdot}4H_2O$ and same amount NaOH was carried out for reference. The XRD results showed that this reaction may lead to the formation of hydrolyzed $Na_2Sn(OH)_6$ and $Na_2SnO_3$ (Eqs. (3)–(5)), and hence, less tin is favorable for doping.

$$4NaOH + SnCl_4 \rightarrow Sn(OH)_4 + 4NaCl \quad (3)$$

$$Sn(OH)_4 + 2NaOH \rightarrow Na_2Sn(OH)_6 \quad (4)$$

$$Na_2Sn(OH)_6 \rightarrow Na_2SnO_3 + 3H_2O \quad (5)$$

### 3.2. Gas sensing properties

All the samples in this work exhibited *n*-type conductivity in the entire working temperature range. The best working temperature for maximum sensitivity was determined for each sample. The gas sensing characteristics of samples S0 to S4 are shown in Fig. 3. It is evident that the introduction of tin leads to an increase in response to ethanol vapor, the sample S4 was observed have the highest gas response. It can be seen from Fig. 3 that the gas response of the sensor in air has a double humped distribution with peaks at 234 and 267 °C, which is typical of the performance of a surface-controlled gas sensor. It is well known that the gas response is the ratio of the resistances of semiconductor in gas and in air, and the resistances will exponentially decrease with the

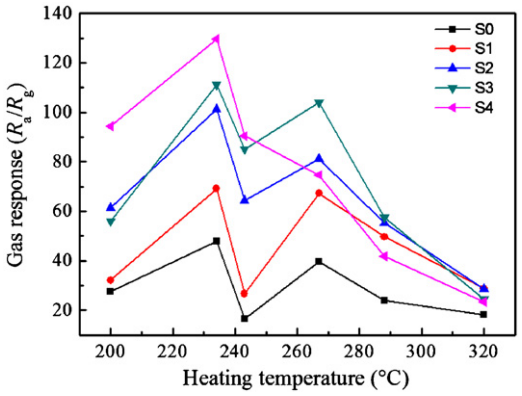


**Fig. 3.** Gas response as a function of different heating temperatures for doped and undoped ZnO gas sensor to ethanol vapor.

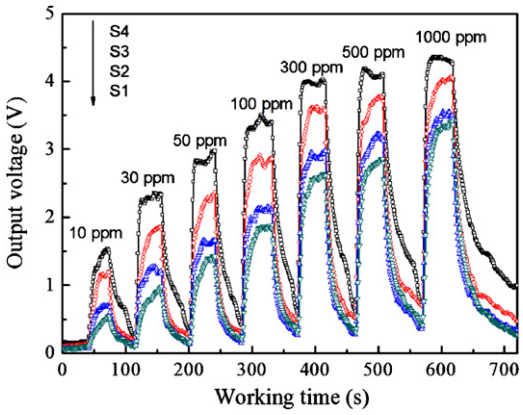


**Fig. 5.** Typical response and recovery curves on cycling between increasing concentration of ethanol vapor and ambient air for different amount of tin-doped ZnO gas sensors.

increase of temperature in air, whilst the resistances will take on different variation characters (camelback or volcano frameworks) because of chemical absorption of various oxygen species on the surface of the gas sensing materials [30]. The increase in resistance is caused by the chemical adsorption of oxygen. The behavior is similar to the surface chemical properties of $SnO_2$ and high resistance will favor the gas response [31]. The transformation may be expressed as $O_2(g) + e^- \Leftrightarrow O_2^-$, $O_2^-(ad) + e^- \Leftrightarrow O_2^{2-}(ad)$. The maximum gas response appears at a lower temperature than is the case of lower doped and undoped samples, and avoid the camelback phenomena. One reason for the fantastic gas response of sample S4 is due to its surface area (9.70 $m^2/g$) which could provide more surface reaction sites for adsorption and transportation of gas molecules, and consequently lead to an increase in electron transfer between tested gas and ZnO flakes. Other samples (S0–S3) showed lower surface areas according to BET results (4.68–6.539 $m^2/g$). The enhancement in the gas sensing properties may come from the hetero junction in tin-doped ZnO photocatalyst, the hetero-contact interface is temperature-dependent [32]. The forward current is greatly increased with increasing temperature which in favor of the gas sensing properties.

The gas response of these materials to gasoline, acetone, heptane, ammonia, carbon monoxide, ethanol vapor and toluene at 234 °C were probed and the results are shown in Fig. 4. The gas response to ethanol vapor is significantly higher than to the other gases and vapors tested, with a magnitude about 54 times greater to 100 ppm ethanol vapor than that for all the other tested gases under the same concentration. In all tested gases, the sensor showed a low response to acetone, ammonia, carbon monoxide, gasoline and toluene, and almost totally insensitive to carbon monoxide. Selectivity is the ratio of gas response to ethanol vapor and to other gases, so the selectivity of the sensor is almost 10 times greater for ethanol vapor. Response and selectivity to ethanol vapor of the sensors can be improved by increasing the content of tin in the ZnO. The above results indicated that the effect of other tested gases on the detection of ethanol vapor is limited due to very low gas response. In other words, the selectivity of the sensor based on sample S4 was very high and the sensor showed high anti-interference ability.

Fig. 5 shows typical response and recovery curves on cycling between increasing concentration of ethanol and ambient air. The output voltage underwent a drastic ascent on the injection of ethanol vapor and was mostly restored to its initial value after the test gas was released. The results are very interesting since the system can readily detect the ethanol vapor concentrations well below the limit imposed for a breathalyzer (e.g. 200 ppm). The stepwise increase in output voltage obtained with increasing ethanol concentration from air to 1000 ppm ethanol gas in air. It can be seen that gas sensor exposed to higher ethanol vapor concentration leads to an output voltage increase. After several cycles of the different concentration of gas injection, full recovery to the initial output voltage of the gas sensors was not achieved in 31 s, possibly due to residual ethanol vapor.

### 3.3. Photocatalytic properties

The photocatalytic activity of the tin-doped ZnO photocatalysts has also been investigated (Fig. 6). Pure ZnO showed poor photocatalytic performance to MO solution, which is in good agreement

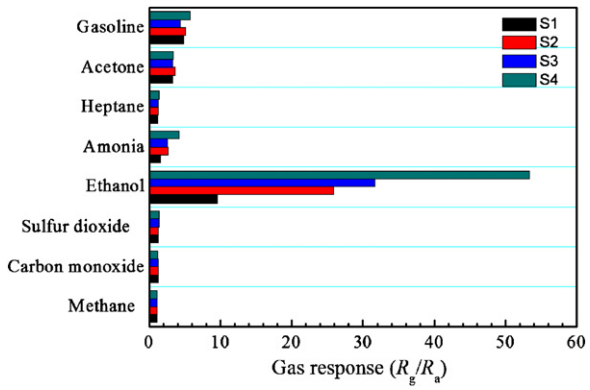


**Fig. 4.** Gas responses of tin-doped ZnO gas sensors to different tested gases when the heating temperature is 234 °C.

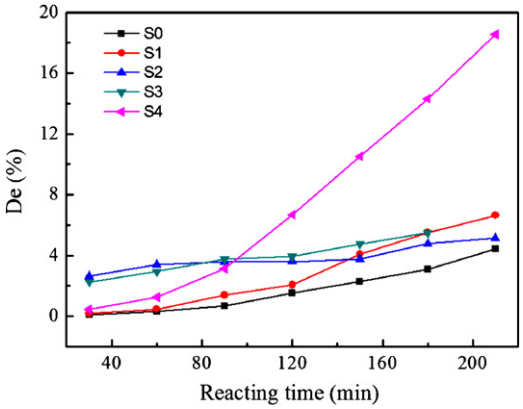


**Fig. 6.** Decolorization rate of methyl orange dye for different oxidation processes by different photocatalysts.

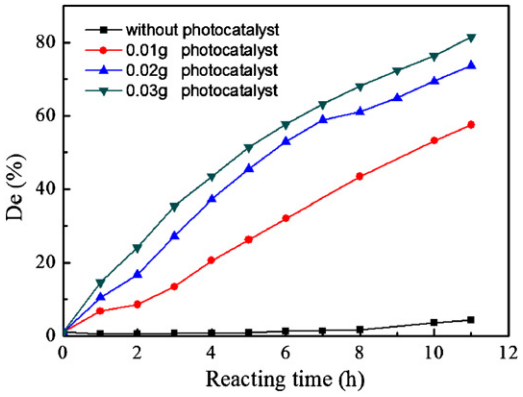


**Fig. 7.** Photocatalytic decolorization of methyl orange solution as a result of different amounts of sample S4 photocatalysts under UV-light irradiation for different time.

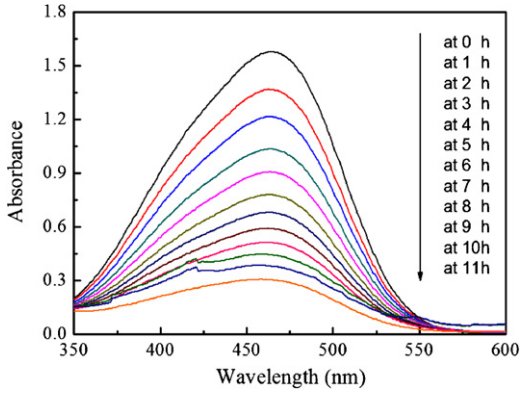


**Fig. 8.** UV–vis absorbance spectra of methyl orange solution during photocatalytic decolorization using sample S4 at different time intervals.

with previous reports [33,34]. The tin content is an important factor to the photocatalytic activity of the doped ZnO material. It is clear that the sample S4 displayed higher photocatalytic activity than all other samples. The photocatalytic activity of the sample S4 is ~10 times than that of pure ZnO. It is known that the fast recombination rate of the photogenerated electron–hole pairs hinders the decolorization of MO. The tin-doped ZnO nanocrystals may increase the photocatalytic efficiency by increasing the charge separation and extending the photoresponding range. In addition, the flake structures were in favor of the transfer of electrons and holes generated inside the crystal to the surface, and facilitated the decolorization of MO solution [35].

The effect of the loading of photocatalyst on the percentage of decolorization of MO is shown in Fig. 7. It clearly shows that the time of the irradiation and the amount of the photocatalyst affect the decolorization of the MO. A blank experiment under UV irradiation without the photocatalyst exhibited no obvious decolorization of the MO solution. It was observed that by increasing photocatalyst loading from 10 mg to 30 mg, the amount of decolorization in a given time also increased. This observation may be caused by the increase in the number of photons absorbed by photocatalyst and/or the number of activated molecules adsorbed on the photocatalyst surface with increase in photocatalyst concentration.

A change in the UV–vis diffusion reflectance spectra (DRS) of the aqueous MO solution during photocatalytic decolorization using the sample S4 is presented in Fig. 8. It is apparent that the intensity of absorption peak gradually decreases with the increasing irradiation time. After UV irradiation for *ca.* 11 h, the intensity of absorption peak of MO aqueous solution is very weak and its solution becomes colorless, indicating near to complete decolorization of MO.

## 4. Conclusions

A facile solid-state synthesis of tin-doped ZnO at room temperature has been introduced. XRD results showed the formation of wurtzitic ZnO. No other phases were detected. The amount of tin added shows a profound effect on morphology which changed from sheet structures (for pure sample) to flakes (for sample S4). As-synthesized doped and undoped ZnO crystals were tested and compared for their photocatalytic activities as well as gas sensing properties. It was clear that sample S4 showed the highest gas response ($R_a/R_g = 124$) to ethanol vapor. The same sample also showed the highest photocatalytic activity toward methyl orange (MO) solution.

## Acknowledgements

This work has been supported by the NCET and 111 Program (B08040) of MOE, Xi'an Science & Technology Foundation (CXY08006, XA-AM-200905) the Fundamental Research Foundation (NPU-FFR-200703), and the SKLSP Research Fund (40-QZ-2009) of China. POB and MA would like to acknowledge EPSRC, UK for financial assistance.

## References

[1] Q.F. Zhou, C. Sharp, J.M. Cannata, K.K. Shung, G.H. Feng, E.S. Kim, Self-focused high frequency ultrasonic transducers based on ZnO piezoelectric films , Appl. Phys. Lett. 90 (2007) 113502-1–113502-3.
[2] N.K. Zayer, R. Greef, K. Rogers, A.J.C. Grellier, C.N. Pannell, In situ monitoring of sputtered zinc oxide films for piezoelectric transducers , Thin Solid Films 352 (1999) 179–184.
[3] T.K. Gupta, Application of zinc oxide varistors , J. Am. Ceram. Soc. 73 (1990) 1817–1840.
[4] C. Panatarani, I.W. Lenggoro, K. Okuyama, The crystallinity and the photoluminescent properties of spray pyrolized ZnO phosphor containing $Eu^{2+}$ and $Eu^{3+}$ ions , J. Phys. Chem. Solids 65 (2004) 1843–1847.
[5] Y.S. Wang, P.J. Thomas, P. O'Brien, Optical properties of ZnO nanocrystals doped with Cd, Mg, Mn, and Fe ions , J. Phys. Chem. B 110 (2006) 4099–4104.
[6] A. Petrellaa, P.D. Cozzolia, M.L. Currib, M. Striccolib, P. Cosmaa, A. Agostiana, photoelectrochemical study on photosynthetic pigments-sensitized nanocrystalline ZnO films , Bioelectrochem. Bioenerg. 63 (2004) 99–102.
[7] A. Becheri, M. Dürr, P.L. Nostro, P. Baglioni, Synthesis and characterization of zinc oxide nanoparticles: application to textiles as UV-absorbers , J. Nanopart. Res. 10 (2008) 679–689.
[8] A. Janotti, C.G. Van de Walle, Oxygen vacancies in ZnO , Appl. Phys. Lett. 87 (2005) 122102-1–122102-3.
[9] F. Tuomisto, K. Saarinen, K. Grasza, A. Mycielski, Observation of Zn vacancies in ZnO grown by chemical vapor transport , Phys. Status Solidi B 243 (2006) 794–798.
[10] A. Hausmann, B. Schallenberger, Z. Atomic, Molecular, and optical physics , J. Phys. B 11 (1978) 269–280.
[11] D.C. Look, J.W. Hemsky, J.R. Sizelove, Residual native shallow donor in ZnO , Phys. Rev. Lett. 82 (1999) 2552–2555.
[12] L. Dai, X.L. Chen, W.J. Wang, T. Zhou, B.Q. Hu, Growth and luminescence characterization of large-scale zinc oxide nanowires , J. Phys.: Condens. Matter. 15 (2003) 2221–2226.
[13] K. Ueda, H. Tabata, T. Kawai, Magnetic and electric properties of transition-metal-doped ZnO films , Appl. Phys. Lett. 79 (2001) 988–990.
[14] S.J. Han, J.W. Song, C.H. Yang, S.H. Park, J.H. Park, Y.H. Jeong, A key to room-temperature ferromagnetism in Fe-doped ZnO:Cu , Appl. Phys. Lett. 81 (2002) 4212–4214.
[15] X.X. Liu, F.T. Lin, L.L. Sun, W.J. Cheng, X.M. Ma, W.Z. Shi, Doping concentration dependence of room-temperature ferromagnetism for Ni-doped ZnO thin films prepared by pulsed-laser deposition , Appl. Phys. Lett. 88 (2006) 062508-1–062508-3.
[16] K.H. Kim, K.C. Park, D.Y. Ma, Structural electrical and optical properties of aluminum doped zinc oxide films prepared by radio frequency magnetron sputtering , J. Appl. Phys. 81 (1997) 7764–7772.
[17] Y.S. Wang, P.J. Thomas, P. O'Brien, Nanocrystalline ZnO with ultraviolet luminescence , J. Phys. Chem. B 110 (2006) 21412–21415.
[18] M. Peiteado, Y. Iglesias, J.D. Frutos, J.F. Fernández, A.C. Caballero, Preparation of ZnO–$SnO_2$ ceramic materials by a coprecipitation method , Bol. Soc. Esp. Ceram. 45 (2006) 158–162.

[19] C. Wang, X.M. Wang, B.Q. Xua, J.C. Zhao, B.X. Mai, P.A. Peng, G.Y. Sheng, J.M. Fu, Enhanced photocatalytic performance of nanosized coupled ZnO/$SnO_2$ photocatalysts for methyl orange degradation , J. Photochem. Photobiol. A: Chem. 168 (2004) 47–52.
[20] K. Govender, D.S. Boyle, P. O'Brien, D. Binks, D. West, D. Coleman, Room-temperature lasing observed from ZnO nanocolumns grown by aqueous solution deposition , Adv. Mater. 14 (2002) 1221–1224.
[21] A. Dodd, A. McKinley, M. Saunders, T. Tsuzuki, Mechanochemical synthesis of nanocrystalline $SnO_2$–ZnO photocatalysts , Nanotechnology 17 (2006) 692–698.
[22] M. Peiteado, Y. Iglesias, J.F. Fernández, J.D. Frutos, A.C. Caballero, Microstructural development of tin-doped ZnO bulk ceramics , Mater. Chem. Phys. 101 (2007) 1–6.
[23] Y. Ortega, P. Fernández, J. Piqueras, Growth and luminescence of oriented nanoplate arrays in tin doped ZnO , Nanotechnology 18 (2007) 115606–115609.
[24] X.S. Fang, C.H. Ye, L.D. Zhang, Y. Li, Z.D. Xiao, Formation and optical properties of thin and wide tin-doped ZnO nanobelts , Chem. Lett. 34 (2005) 436–437.
[25] J.B. Wiley, R.B. Kaner, Rapid solid-state precursor synthesis of materials , Science 255 (1992) 1093–1097.
[26] J.Q. Xu, X.H. Jia, X.D. Lou, G.X. Xi, J.J. Han, Q.H. Gao, Selective detection of HCHO gas using mixed oxides of ZnO/$ZnSnO_3$ , Sens. Actuators B 120 (2007) 694–699.
[27] X.D. Lou, X.H. Jia, J.Q. Xu, S.Z. Liu, Q.H. Gao, Hydrothermal synthesis, characterization and photocatalytic properties of $Zn_2SnO_4$ nanocrystal , Mater. Sci. Eng. A 432 (2006) 221–225.
[28] S.Y. Li, P. Lin, C.Y. Lee, T.Y. Tseng, C.J. Huang, Effect of Sn dopant on the properties of ZnO nanowires , J. Phys. D: Appl. Phys. 37 (2004) 2274–2282.
[29] U. Pal, P. Santiago, Controlling the morphology of ZnO nanostructures in a low-temperature hydrothermal process , J. Phys. Chem. B 109 (2005) 15317–15321.
[30] J.Q. Xu, X.H. Wang, C. Li, Electrochemical-deposited $In_2O_3$ nanocrystals for $H_2S$ detecting in air , Solid-State Lett. 9 (2006) H53–H56.
[31] G. Heiland, Homogeneous semiconducting gas sensors , Sens. Actuators 2 (1982) 343–361.
[32] S. Mridha, D. Basak, Investigation of a p-CuO/n-ZnO thin film heterojunction for $H_2$ gas-sensor applications , Semicond. Sci. Technol. 21 (2006) 928–932.
[33] M.R. Hoffmann, S.T. Martin, W.Y. Choi, D.W. Bahnemann, Environmental applications of semiconductor photocatalysis , Chem. Rev. 95 (1995) 69–96.
[34] A. Hagfeldt, M. Gratzel, Light-induced redox reactions in nanocrystalline systems , Chem. Rev. 95 (1995) 49–68.
[35] L. Zhang, D.R. Chen, X.L. Jiao, Monoclinic structured $BiVO_4$ nanosheets: hydrothermal preparation, formation mechanism, and coloristic and photocatalytic properties , J. Phys. Chem. B 110 (2006) 2668–2673.